

ZnO Substitution in Argyrodite $\text{Li}_{5.5+3x}\text{Zn}_x\text{P}_{1-x}\text{O}_x\text{S}_{4.5-x}\text{Br}_{1.5}$ Electrolyte with Enhanced Interface Performance for All-Solid-State Battery

Xizhong Lin,^[a] Dabing Li,^[a] Yaru Li,^[a] Xiaoxue Zhao,^[a] Yang Li,^[a] and Li-Zhen Fan^{*[a]}

Argyrodite sulfide solid electrolytes (SSEs) have been attracting more concentration in ionic conductivity, crystal structure, and mechanical properties. Nevertheless, shortcomings of SSEs like poor air-vapor stability and interface reactions limit the wider application in batteries. Herein, a double-element ZnO substitution strategy is applied to enhancing $\text{Li}_{5.5}\text{PS}_{4.5}\text{Br}_{1.5}$ Argyrodite electrolyte structure stability and property, $\text{Li}_{5.5}\text{PS}_{4.5}\text{Br}_{1.5}$ electrolyte with a small amount of ZnO substitution to P and S. $\text{Li}_{5.5+3x}\text{Zn}_x\text{P}_{1-x}\text{O}_x\text{S}_{4.5-x}\text{Br}_{1.5}$ solid electrolytes have achieved improved performance, interface composition also has changed, and crystal structure is becoming more stable. Specifically, $\text{LPSBr}_{1.5}\text{-}4\%\text{ZnO}$ exhibits the most promising comprehensive properties, more expanded lithium pathway and crystal cell

size, 2.25 mScm^{-1} ionic conductivity at 25°C , 65% electronic conductivity decline, and air stability enhancement. Moreover, $\text{LPSBr}_{1.5}\text{-}4\%\text{ZnO}$ show decent lithium compatibility and dendrite suppression capability, $\text{LPSBr}_{1.5}\text{-}4\%\text{ZnO}$ can continue cycling for more than 800 h at 0.1 mA cm^{-2} in Li symmetric cell, and critical current density has reached 1.4 mA cm^{-2} . More importantly, an all-solid-state battery (ASSB) with $\text{LPSBr}_{1.5}\text{-}4\%\text{ZnO}$ electrolyte can cycle with 130 mAh g^{-1} capacity and more than 120 cycles in $\text{LiCo}_2|\text{SSE}|\text{In-Li}$ cell. Our work might provide a strategy to promote structure stability and electrochemical durability, and how element substitution affects ionic transport pathway and crystal structure.

Introduction

Energy consumption develops rapidly, and more efficient and advanced energy storage devices and materials are required urgently. Lithium-ion batteries have played a more vital role in energy conversion and storage at present.^[1-2] Nevertheless, in liquid lithium-ion batteries, several disturbing shortcomings of liquid electrolytes such as limited energy density (less than 300 Wh kg^{-1}),^[3] safety concerns caused by flammable electrolytes, and cell short circuits come from serious lithium dendrite growth,^[4] all of them suppress the larger-scale application. Spontaneously, solid electrolyte replacing the liquid electrolyte might solve these difficulties and concerns. Nonflammable solid electrolytes can enable assembly with high-capacity intercalation cathodes,^[5] alloy anodes,^[6] or lithium anode. In addition to providing higher energy density (greater than 400 Wh kg^{-1}), and inhibiting the lithium dendrite growth.^[7]

Currently, solid electrolytes can be classified into two categories generally, organic polymer and inorganic solid electrolyte. Sulfide solid electrolyte (SSE) possesses the highest ionic conductivity and suitable mechanical properties in all inorganic electrolytes.^[8] Sulfide solid electrolytes provide higher ionic conductivity for the smaller electronegativity, lower bond

energy to Li ions, and a bigger atomic radius.^[9] Indeed, the high ionic conductivity of solid electrolytes is a positive factor for future application in all-solid-state battery (ASSB), and the ionic conductivity of SSEs even surpasses traditional liquid electrolytes (10 mScm^{-1}). $\text{Li}_{10}\text{GeP}_2\text{S}_{12}$ solid electrolyte was reported an ionic conductivity of 12 mScm^{-1} ,^[10] and ionic conductivity of $\text{Li}_{9.54}\text{Si}_{1.74}\text{P}_{1.44}\text{S}_{11.7}\text{Cl}_{0.3}$ even reached 25 mScm^{-1} .^[11] Recently, Kanno^[12] found that a $\text{Li}_{9.54}(\text{Si}_{0.6}\text{Ge}_{0.4})_{1.74}\text{P}_{1.44}\text{S}_{11.1}\text{Br}_{0.3}\text{O}_{0.6}$ electrolyte has an ionic conductivity of 32 mScm^{-1} at 25°C . In addition, Argyrodite sulfide solid electrolytes have also been attracting more concentration due to their preferable ionic conductivity, the stable face center cubic (FCC) crystal structure, and three familiar lithium-conducting pathways (inter-cage jump, intra-cage jump, double jump).^[8] Moreover, $\text{Li}_6\text{PS}_5\text{Br}$ has boasted the lowest activation barriers for ionic conductivity in the halide Argyrodite family,^[13] and exhibits a low ionic conductivity for 1.1 mScm^{-1} at 25°C .^[14] Density functional theory shows that the fully ordered structure is the most thermodynamically stable configuration. Furthermore, the site disorder strategy has been applied in Argyrodite SSEs to improve their ionic conductivities.^[15-17] A higher degree of site disorder means more spatially distributed Li^+ and shorter Li^+-Li^+ distances responsible for the inter-cage jumps.^[18] The optimized site disorder can subsequently lead to an ionic conductivity increase, and a higher disorder degree enables better Li^+ transport.^[19] Sun developed a Bromine-rich Argyrodite $\text{Li}_{5.5}\text{PS}_{4.5}\text{Br}_{1.5}$,^[20] and a cold-pressed $\text{Li}_{5.5}\text{PS}_{4.5}\text{Br}_{1.5}$ pellet has a high ionic conductivity of 4.38 mScm^{-1} at 25°C . Because Br ion (196 pm) has a similar ionic radius to S ion (184 pm), the mixed S/Br state can form easily. Nevertheless, electrochemical performance relies not only on high ionic conductivity but also

[a] X. Lin, D. Li, Y. Li, X. Zhao, Y. Li, Prof. Dr. L.-Z. Fan
Beijing Advanced Innovation Center for Materials Genome Engineering,
Institute of Advanced Materials and Technologies
University of Science and Technology Beijing
Beijing 100083, China
E-mail: fanlizhen@ustb.edu.cn

 Supporting information for this article is available on the WWW under
<https://doi.org/10.1002/batt.202400048>

on the stability of the interface of electrolyte and electrode.^[21] Site disorder improves the ionic conductivity of SSEs. At the same time, site disorder crystal structures might suffer from more serious interface reactions and electrolyte decomposition.^[18] Moreover, several other weaknesses also limit the further application of SSEs, almost all sulfide solid electrolytes are unstable in the air atmosphere, and exhibit a relatively narrow electrochemical stability window.^[22] In addition, the microstructure of the electrode and electrolyte can induce large impedance in the cell.^[23]

Many methods have been developed to mitigate the above shortcomings, like oxygen element substitution in $\text{Li}_6\text{PS}_{5-x}\text{O}_x\text{Br}$ electrolyte,^[24] material coating,^[25] organic-inorganic composite,^[26-27] and multi-layer electrolyte.^[28] The material direct coating is challenging due to the high crystallization temperature and uneven coating layer.^[29] Composite electrolytes and multi-layer electrolytes might lead to extra interfaces and extra interface reactions. One of the most typical methods to enhance the moisture stability of solid electrolytes is elemental site substitution, which can change the atom composition, crystal structure, and cell parameters. In addition, the substitution process can be achieved during the electrolyte preparation procedure, which is convenient for mass production for its concise operation. Lately, our group has revealed the improvement of ionic conductivity, moisture stability, interface performance, and other vital performances in $\text{Li}_6\text{PS}_5\text{Cl}$,^[30-31] Li_3PS_4 ,^[32] through Bi_2O_3 or Sb element substitution. Other compounds like Sn–O substitution in LPSI,^[33] $\text{Li}_7\text{P}_3\text{S}_{11}$,^[34] and Nb–O substitution in $\text{Li}_7\text{P}_3\text{S}_{11}$ solid electrolytes performance have been characterized thoroughly.^[35] Moreover, Pr has also been applied in the single-crystal cathode.^[36] The results exhibit enhanced performance and interface stability improvement. Nevertheless, the property enhancement mechanisms in ionic conduction, chemical stability, interface composition, and ASSB performance are revealed insufficiently. Though element substitution on ordered site SSEs arrangement is widely reported such as LPS,^[37-39] LPSI,^[40-41] LPSBr.^[24,42-43] Nevertheless, element substitution in site-disordered SSEs is a few,^[44-46] for its complex and unstable crystal structure. All of the above examples show options for us.

In this work, enlightened by substitution strategy. Air-stable, high voltage-stable oxygen (O) and lithium-affinity zinc (Zn) are used to substitute phosphorus (P) and sulfur (S) in $\text{Li}_{5.5}\text{PS}_{4.5}\text{Br}_{1.5}$, to improve the stability and sustainability. $\text{Li}_{5.5}\text{PS}_{4.5}\text{Br}_{1.5}$ exhibits higher ionic conductivity than $\text{Li}_6\text{PS}_5\text{Br}$, but it is chemically unstable with lithium metal.^[20] This ZnO substitution method combines the advantages of high ionic conductivity and stable performance. The former stems from site disorder and the latter stems from element substitution. Experimental and result analyses are conducted to understand the role of substitution, and fast lithium-ion transport performance in site-disorder electrolyte $\text{Li}_{5.5}\text{PS}_{4.5}\text{Br}_{1.5}$ with varying substitution amounts. LPSBr_{1.5}-4%ZnO electrolyte shows superior comprehensive properties by comparison. The ionic conductivity reached 2.25 mS cm^{-1} at 25°C , this value is 2.25 orders higher than the parent phase $\text{Li}_6\text{PS}_5\text{Br}$.^[14] Superior interfacial stability, lithium compatibility, and lithium dendrite inhibition capability have

been achieved in cells assembled with LPSBr_{1.5}-4%ZnO electrolyte, and Li symmetric cell exhibits small over-potential and little resistance growth. In addition, ASSB with LPSBr_{1.5}-4%ZnO electrolyte enables good discharge capacity and decent capacity capability. It can be admitted that ZnO is a superior substitution for site-disordered electrolytes.

Results and Discussion

In this work, a series of $\text{Li}_{5.5+3x}\text{Zn}_x\text{P}_{1-x}\text{O}_x\text{S}_{4.5-x}\text{Br}_{1.5}$ sulfide electrolytes are systematically synthesized and characterized. As shown in Figure S1, electrolytes are synthesized through ball-milling and thermal annealing by the familiar procedure.^[20] Figure 1a shows X-ray diffraction (XRD) patterns of the $\text{Li}_{5.5+3x}\text{Zn}_x\text{P}_{1-x}\text{O}_x\text{S}_{4.5-x}\text{Br}_{1.5}$ electrolytes ($0 \leq x \leq 0.08$), which correspond well with the original parent pattern of $\text{Li}_{5.5}\text{PS}_{4.5}\text{Br}_{1.5}$ ($\text{Li}_{5.5}\text{PS}_{4.5}\text{Br}_{1.5}$ is abbreviated as LPSBr_{1.5}, $\text{Li}_{5.62}\text{Zn}_{0.04}\text{P}_{0.96}\text{O}_{0.04}\text{S}_{4.46}\text{Br}_{1.5}$ is abbreviated as LPSBr_{1.5}-4%ZnO for convenience, other samples also follow this way). The intensity of peaks at $2\theta = 30^\circ$, 52.3° decreases with increasing ZnO introduction, and peaks at $2\theta = 25.5^\circ$, 47.8° of LPSBr_{1.5} almost disappear at LPSBr_{1.5}-xZnO. Diffraction peaks at $2\theta = 22.2^\circ$, 65.7° , 70.2° , and 74.6° correspond to LiBr (PDF-49-0959). It is not nonreasonable that peaks of LiBr appear in Br-rich Argyrodite electrolytes. At the same time, the detailed XRD patterns graph of LPSBr_{1.5}-xZnO shows a slight peak moving to a higher degree. Inducing by Bragg law $2d\sin\theta = n\lambda$, higher degree moving illustrates a lattice contraction. Nevertheless, LPSBr_{1.5}-4%ZnO has a similar peak position with LPSBr_{1.5}, indicating a similar electrolyte lattice expansion by a specific ZnO amount. In addition, O^{2-} (140 pm) has a smaller size than that of S^{2-} (184 pm), the introduction of oxygen will form the P–O bond or $\text{PS}_{4-x}\text{O}_x^{3-}$ group, which occupies a smaller octahedron site and provide more space for the Li diffusion. Consequently, the crystal parameter has changed due to ZnO substitution, oxygen incorporation might provide a bigger crystal lattice and broader Li diffusion pathways. It can be admitted that LPSBr_{1.5}-4%ZnO possesses fantastic performance in LPSBr_{1.5}-xZnO series electrolytes. Besides, no impurity peaks appearance suggests the successful ZnO substitution to the electrolyte composition. There are no characteristic peaks of elemental Zn, indicating that ZnO did not agglomerate into a new phase, the ZnO is composed of the electrolyte structure, and the solid-phase synthesis is effective. Indeed, the LPSBr_{1.5} electrolyte also exhibits a decent ZnO solid-solution limit due to similar XRD patterns. ZnO can modify the structure, react with free $\text{S}^{2-}/\text{Br}^-$ ions, and construct the cubic structure and lithium pathway jointly. Moreover, as shown in supplementary Figure S2. By comparing the X-ray diffraction (XRD) peaks of ZnO mixing with LPSBr_{1.5} and LPSBr_{1.5}-4%ZnO. XRD pattern of ZnO mixing LPSBr_{1.5} exhibits a simple superposition of the two characteristic peaks. In three strong peaks of ZnO (15.9° , 17.2° , 18.1°), only ZnO mixing LPSBr_{1.5} electrolyte appears to peak at 15.9° , which indicates that ZnO participates in the crystal construction by ball-milling, and ZnO mixing LPSBr_{1.5} have an inferior incorporation effect than ball-milling. Raman spectroscopy is performed to reveal the effect of ZnO substitution on

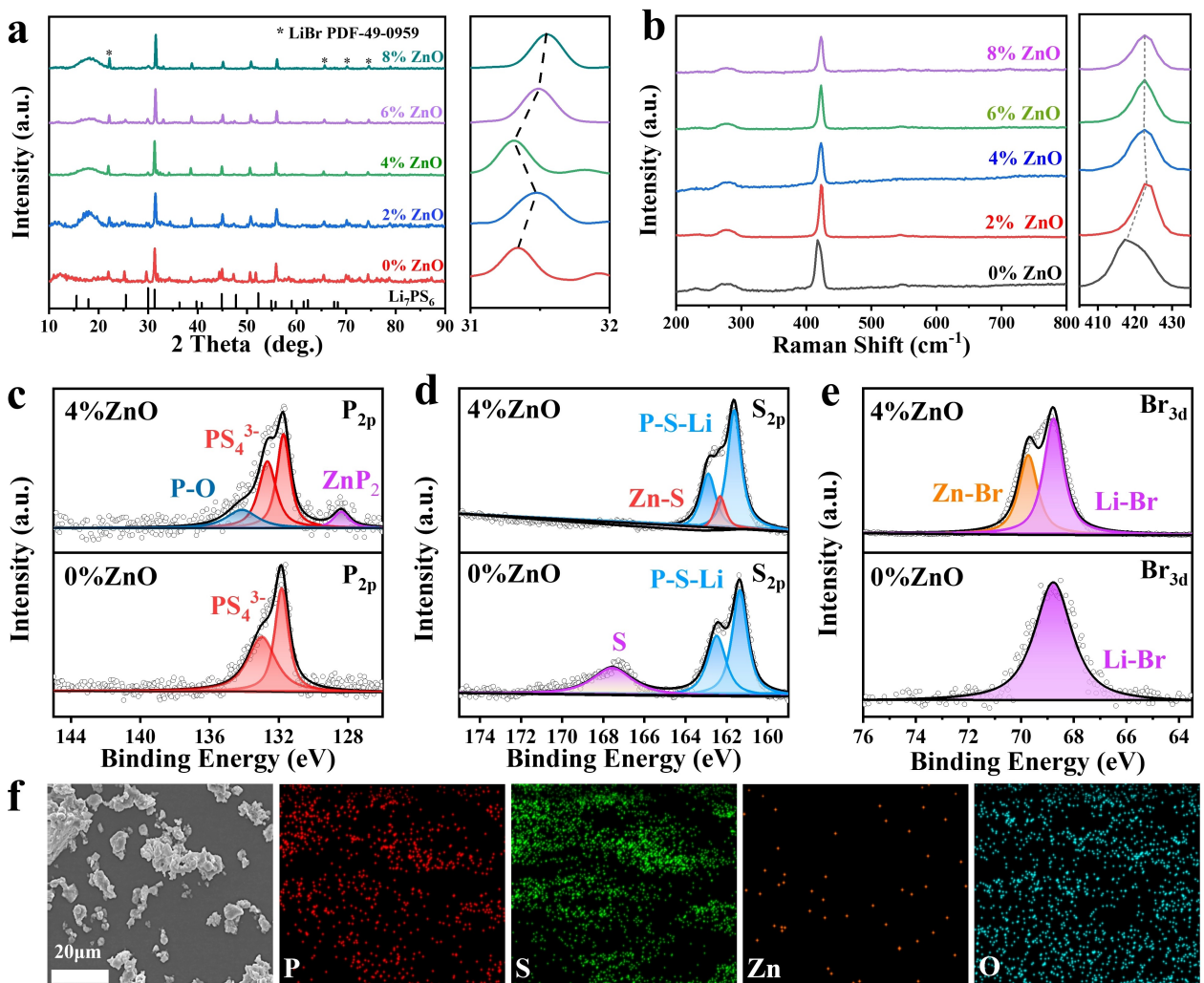


Figure 1. Structure characterization and analysis of $\text{Li}_{5.5+3x}\text{Zn}_x\text{P}_{1-x}\text{O}_x\text{S}_{4.5-x}\text{Br}_{1.5}$ electrolytes, $x = 0, 0.02, 0.04, 0.06, 0.08$. (a) XRD patterns of $\text{Li}_{5.5+3x}\text{Zn}_x\text{P}_{1-x}\text{O}_x\text{S}_{4.5-x}\text{Br}_{1.5}$ electrolytes with detail comparison graph, (b) Raman spectra of $\text{Li}_{5.5+3x}\text{Zn}_x\text{P}_{1-x}\text{O}_x\text{S}_{4.5-x}\text{Br}_{1.5}$ electrolytes with detail comparison. XPS spectra comparison of (c) P_{2p} , (d) S_{2p} , (e) Br_{3d} in $\text{LPSBr}_{1.5}$ and $\text{LPSBr}_{1.5}-4\%\text{ZnO}$ electrolyte. (f) SEM images for $\text{LPSBr}_{1.5}-4\%\text{ZnO}$ electrolyte with corresponding EDS mappings of P, S, Zn, O.

the $\text{LPSBr}_{1.5}$ electrolyte structure. As shown in Figure 1b, the peak at 418 cm^{-1} of PS_4^{3-} group all exhibit a slightly equal moving to higher wavenumber (424 cm^{-1}) in $\text{LPSBr}_{1.5}-x\text{ZnO}$ electrolytes, equal moving suggests the stable $\text{PS}_{4-x}\text{O}_x^{3-}$ group formation and equal changes in microstructure occurred in $\text{LPSBr}_{1.5}-x\text{ZnO}$ electrolytes. ZnO stabilizes the site-disordered crystal structure and improves stability.

X-ray photoelectron spectrum (XPS) spectra comparison of (c) P_{2p} , (d) S_{2p} , (e) Br_{3d} in $\text{LPSBr}_{1.5}$ and $\text{LPSBr}_{1.5}-4\%\text{ZnO}$ electrolyte are shown in Figure 1c–e. The bond environment of P, S, and Br elements all change obviously among $\text{LPSBr}_{1.5}$ and $\text{LPSBr}_{1.5}-4\%\text{ZnO}$, a more stable bond environment forms due to the introduction of minor oxygen and Zinc element. In P_{2p} XPS spectra of $\text{LPSBr}_{1.5}-4\%\text{ZnO}$ (Figure 1c), ZnP_2 (128.1 eV) bond has formed (citing from NIST X-ray Photoelectron Spectroscopy Database), stable $\text{P}-\text{O}$ bond (134.5 eV) also forms due to ZnO introduction. Moreover, peaks at 130.9 eV and 132.5 eV correspond to the $\text{P}-\text{S}$ bond. In XPS spectra of S_{2p} (Figure 1d), the newly formed peak at 162.1 eV in $\text{LPSBr}_{1.5}-4\%\text{ZnO}$ is related to

the $\text{Zn}-\text{S}$ bond, which can contribute to the stable structure. 162.4 eV is related to the $\text{P}-\text{S}$ bond and 161.2 eV is related to the $\text{P}=\text{S}$.^[31] XPS spectra peak of S_{2p} has a shoulder peak, both of them represent the $\text{Li}-\text{P}-\text{S}$ bond.^[31] The peak at 167.8 eV in $\text{LPSBr}_{1.5}$ corresponds to the free S element (S_0) and disappears in $\text{LPSBr}_{1.5}-4\%\text{ZnO}$ at the same position. In XPS spectra of Br_{3d} (Figure 1e), the $\text{Zn}-\text{Br}$ (70.0 eV) bond has formed uniquely in $\text{LPSBr}_{1.5}-4\%\text{ZnO}$, $\text{Li}-\text{Br}$ (69.2 eV) bond appears at $\text{LPSBr}_{1.5}$ and $\text{LPSBr}_{1.5}-4\%\text{ZnO}$. To conclude, newly formed $\text{P}-\text{O}$, ZnP_2 , $\text{Zn}-\text{S}$, and $\text{Zn}-\text{Br}$ bonds in $\text{LPSBr}_{1.5}-4\%\text{ZnO}$ provide a new bond composition and a stable structure. As shown in Figure S3, XPS spectra comparison of O_{1s} in $\text{LPSBr}_{1.5}$ and $\text{LPSBr}_{1.5}-4\%\text{ZnO}$ electrolyte both have peaked at 531.5 eV. The oxygen element in the $\text{LPSBr}_{1.5}$ sample might come from air while testing.

Scanning electron micrograph (SEM) images and corresponding energy dispersive spectral (EDS) mappings for $\text{LPSBr}_{1.5}-4\%\text{ZnO}$ electrolyte are shown in Figure 1f. The smaller electrolyte particles ($5-10 \mu\text{m}$) can provide higher surface area, more abundant interfacial contacts in the composite cathode,

and form tight contact in electrolyte layer for achieving a better ionic conduction net. It can be indicated that the introduced ZnO has a wide disperse in substituted electrolytes. The oxygen amount is much higher than the zinc amount in EDS mapping, which might be due to the reaction between the electrolyte and moisture in the air during SEM testing.

Ionic conductivity is an important index in electrolytes. The ionic conductivity of $\text{Li}_{5.5+3x}\text{Zn}_x\text{P}_{1-x}\text{O}_x\text{S}_{4.5-x}\text{Br}_{1.5}$ ($0 \leq x \leq 0.08$) is induced by electrochemical impedance spectroscopy (EIS), and Nyquist plots are shown in Figure S4a. Ionic conductivities of $\text{LPSBr}_{1.5-x}\text{ZnO}$ follow the sequence of $0\% > 2\% > 4\% > 6\% > 8\%$ ZnO substitution amount. Oxygen element introduction leads to the ionic conductivity of electrolytes decrease, oxygen has a larger electronegativity than sulfur, which limits the fast Li^+ migration. Nevertheless, the decrease was compensated by Zn introduction, zinc element has expanded the ionic conductivity pathway, therefore, the ionic conductivity decreases mildly. In addition, the sintering process has been proven a vital effect on ionic conductivity enhancement. The ionic conductivity of annealed (Figure S4b) $\text{Li}_{5.5}\text{PS}_{4.5}\text{Br}_{1.5}$ reaches 4.39 mS cm^{-1} , which corresponds well with the literature.^[20] The ball-milled $\text{Li}_{5.5}\text{PS}_{4.5}\text{Br}_{1.5}$ electrolyte shows 0.27 mS cm^{-1} ionic conductivity. The ionic conductivity (IC) is upgraded about 16 times through sintering, and (Figure S4c) $\text{LPSBr}_{1.5-4\%}\text{ZnO}$ is similar. The SSE powder has formed the Li-conducting phase by ball-milling, but it still has many grain boundaries and high impedance. The sintering process might homogenize the electrolyte, reduce the grain boundary impedance, and increase the ionic conductivity. Figure 2a shows the varying-temperature Arrhenius plots, temperature ranges from 25°C to 80°C at an interval of 5°C . The electronic conductivity curves of $\text{LPSBr}_{1.5-x}\text{ZnO}$ ($0 \leq x \leq 0.08$) are shown in Figure 2b, the electronic conductivity of $\text{LPSBr}_{1.5-4\%}\text{ZnO}$ is determined to be $1.17 \times 10^{-8} \text{ S cm}^{-1}$ measured by direct-current polarization, which has decreased by 65% compared to $\text{LPSBr}_{1.5}$ ($3.38 \times 10^{-8} \text{ S cm}^{-1}$), and Figure S5 shows the detail of electronic conductivity curves at 2000–2400 s. The high electronic conductivity of $\text{Li}_7\text{La}_3\text{Zr}_2\text{O}_{12}$ and Li_3PS_4 electrolytes is mostly responsible for dendrite formation.^[47] Therefore, low electronic conductivity is conducive to inhibiting the growth of dendrites and improving the electrolyte stability of lithium. Figure 2c shows the ionic conductivities variation and

activation energy (E_a) variation of $\text{LPSBr}_{1.5-x}\text{ZnO}$ at 25°C with various substitution proportions. The ionic conductivities show a slight decrease when the ZnO substitution amount increases and the ionic conductivity of the $\text{LPSBr}_{1.5-4\%}\text{ZnO}$ is determined to be 2.25 mS cm^{-1} at 25°C . ZnO reduces the site-disorder degree, such as free sulfur element. In addition, the basic ionic conductivity mechanism (inter-cage jump, intra-cage jump, double jump) is not influenced by ZnO substitution, due to minor ionic conductivity variance. Even though $\text{LPSBr}_{1.5-4\%}\text{ZnO}$ has approximately a 50% ionic conductivity loss compared with $\text{LPSBr}_{1.5}$, $\text{LPSBr}_{1.5-4\%}\text{ZnO}$ can also be used in the solid-state battery for its high ionic conductivity, because it is 2.25 orders higher than the Argyrodite phase LPSBr .^[14] It is not unreasonable that a 50% ionic conductivity decline occurs due to oxygen substitution.

Furthermore, extra Li^+ (about three times of ZnO amount) is introduced into the electrolyte for electric neutrality. Excessive Li^+ results in sufficient carriers, which is beneficial for ionic conductivity. Aliovalent substitution provides additional Li ions to decrease high-energy lattice sites, which expands an inter-cage migration channel and activates concerted migration.^[48] According to the Arrhenius equation,^[32] changes in the activation energy have an opposite tendency relationship with changes in ionic conductivity, and the larger activation energy would improve the stability of the electrolyte. Series of $\text{LPSBr}_{1.5-x}\text{ZnO}$ all exhibit more stable thermodynamic properties. After 4%ZnO substitution, the increase stabilizes in activation energy variation and changes in ionic conductivity. It can be concluded that $\text{LPSBr}_{1.5-4\%}\text{ZnO}$ possesses a much better comprehensive property among ionic conductivity, electric conductivity, structure lattice, and activation energy (0.31 eV).

Therefore, $\text{LPSBr}_{1.5-4\%}\text{ZnO}$ is regarded as the selected material to investigate the electrochemical performance in the $\text{LPSBr}_{1.5-x}\text{ZnO}$ series. Furthermore, in the above-mentioned pieces of literature,^[33–34] the same substitution element in varying electrolytes results in various ionic conductivity changes in the final solid electrolytes. Influence factors are various, purity of raw materials, experiment equipment characterization, and even experiment skills of laboratory operators, so that the results are various but conclusions are similar. It can be anticipated that the condition would be mitigated by more

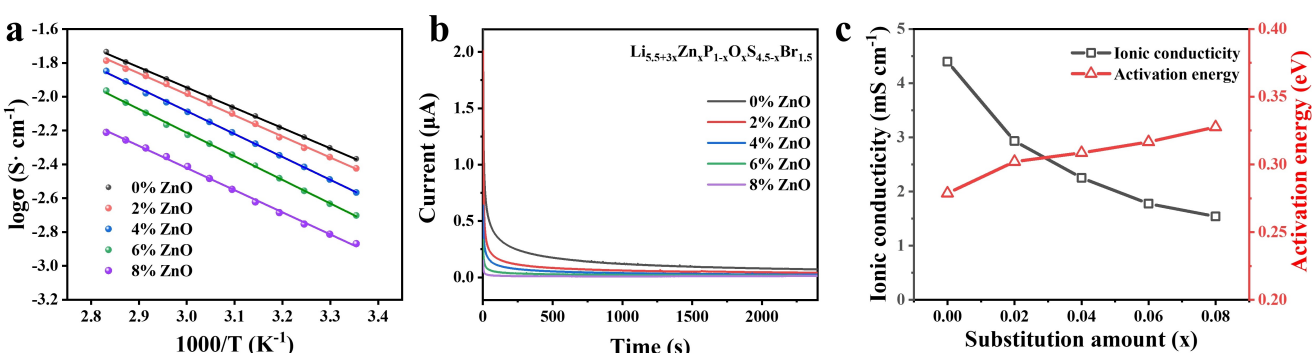


Figure 2. Fundamental electrochemical characterization of $\text{Li}_{5.5+3x}\text{Zn}_x\text{P}_{1-x}\text{O}_x\text{S}_{4.5-x}\text{Br}_{1.5}$ electrolytes, $x = 0, 0.02, 0.04, 0.06, 0.08$. (a) Arrhenius profiles of milled-annealed $\text{Li}_{5.5+3x}\text{Zn}_x\text{P}_{1-x}\text{O}_x\text{S}_{4.5-x}\text{Br}_{1.5}$ electrolytes. (b) Electronic conductivity characterization curves of $\text{Li}_{5.5+3x}\text{Zn}_x\text{P}_{1-x}\text{O}_x\text{S}_{4.5-x}\text{Br}_{1.5}$ electrolytes by direct-current polarization at 0.4 V. (c) Ionic conductivity and activation energy variance diagram in $\text{Li}_{5.5+3x}\text{Zn}_x\text{P}_{1-x}\text{O}_x\text{S}_{4.5-x}\text{Br}_{1.5}$ electrolytes.

standard raw materials, more accurate experiment equipment, and result analysis.

To examine the changes in lithium compatibility property after Zn and O substitution, the Li|SSE|Li symmetric cell is assembled with LPSBr_{1.5} and LPSBr_{1.5}-4%ZnO electrolyte. As illustrated in Figure 3a, LPSBr_{1.5} can only cycle for 200 h with serious polarization, and then a short circuit happens. The site-disorder structure of LPSBr_{1.5} can hardly resist lithium dendrite growth and electrolyte destruction caused by dendrites in cells. The polarization voltage increases continuously in the symmetric cell with LPSBr_{1.5} electrolyte, which results in cell short circuits ultimately. In contrast, a symmetric cell with LPSBr_{1.5}-4%ZnO shows excellent stability with Li metal. The Li|SSE|Li symmetric cell with LPSBr_{1.5}-4%ZnO has cycled for more than 800 h without significant polarization at 0.1 mA cm⁻², promoting an even Li plating and stripping process. Galvanostatic charge-discharge curves at (a1) 30–35 h and (a2) 700–705 h also demonstrate the stable structure of electrolyte in Figure 3. The overpotential of Li|LPSBr_{1.5}-4%ZnO|Li increases from 9 mV to 13 mV after 700 h. Minor cell resistance increases from 114 Ω to 165 Ω, indicating that an existing stable interface inhibits the

serious interface reaction. The initial polarization voltage of LPSBr_{1.5}-4%ZnO is similar to that of LPSBr_{1.5}, which means that the impedance of the two SSEs is also similar. Consequently, the introduced ZnO inhibits the growth of lithium dendrites and destroys the dendrite growth channel. This enhancement is induced by the decrease of S²⁻/Br⁻ site disorder degree and the increase of Li⁺ concentration through the aliovalent cation substitution. The increase in ionic conductivity is not necessary to improve the cycle stability of Li symmetric cells,^[44] and vice versa, the slight decrease in ionic conductivity is not necessary to deteriorate the cycle stability in the cell. Furthermore, the critical current density (CCD) test is operated in a Li symmetric cell with SSEs under an elevated current density with an interval of 0.1 mA cm⁻². As shown in Figure 3d. The upper-limit current density even reaches 1.4 mA cm⁻² for LPSBr_{1.5}-4%ZnO, surpassing all other substituted-electrolytes, which is almost 3 times larger than the upper-limit current density of LPSBr_{1.5} (0.5 mA cm⁻²) in Figure 3b. Figure 3c and Figure 3e show the curves of LPSBr_{1.5}-2%ZnO (0.7 mA cm⁻²) and LPSBr_{1.5}-6%ZnO (0.8 mA cm⁻²), Figure 3f shows the curves of LPSBr_{1.5}-8%ZnO (0.7 mA cm⁻²) in Li symmetric cell. The diagram of critical

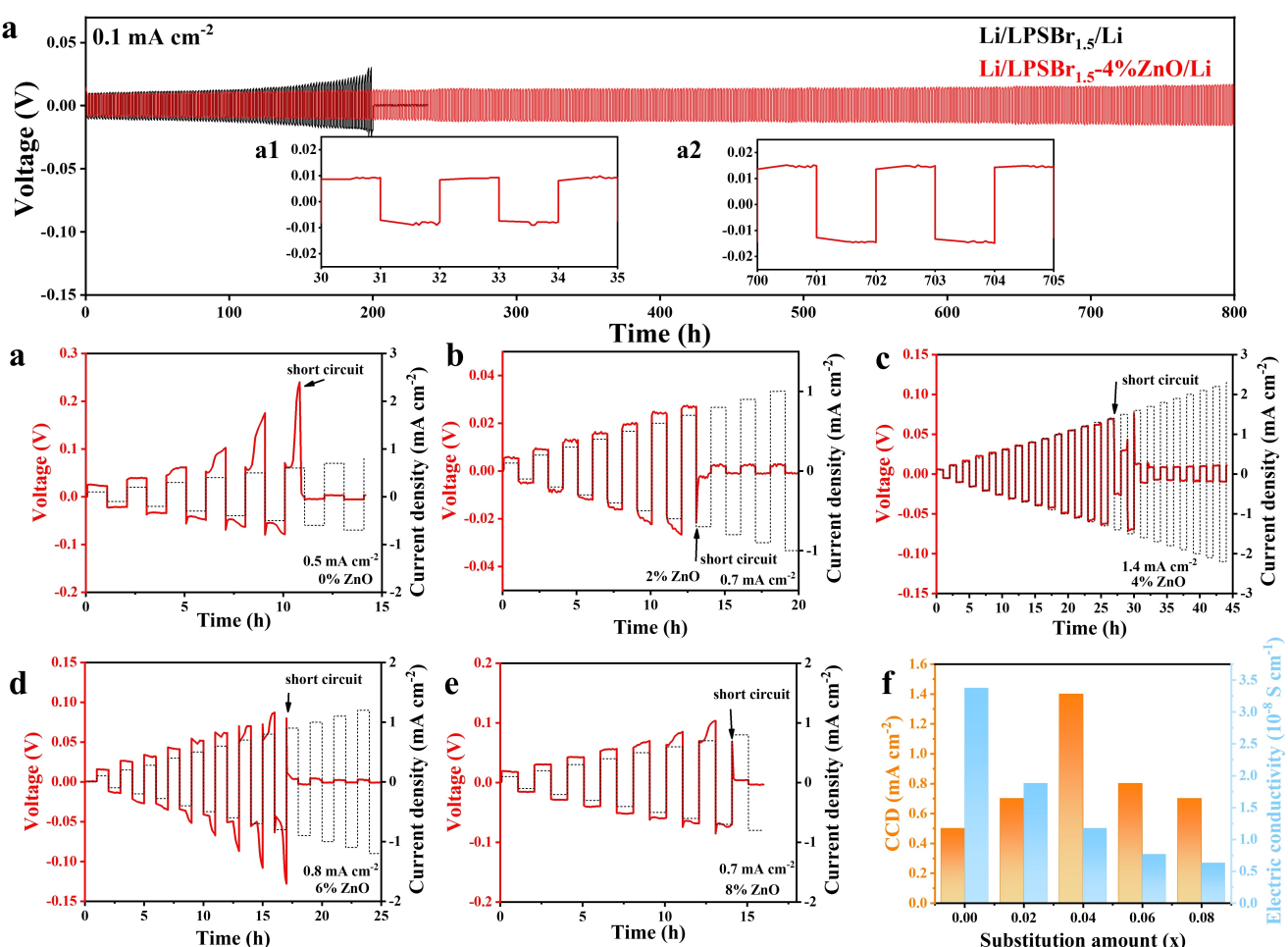


Figure 3. Lithium compatibility and interface stability performance. (a) long-term cycling performance of Li|SSE|Li symmetric cell Galvanostatic charge-discharge curves at 0.1 mA cm⁻² current density, specific time part (a1) 30–35 h, (a2) 700–705 h, (SSE: LPSBr_{1.5} and LPSBr_{1.5}-4%ZnO). Curves of symmetric cell performance with 0.1 mA cm⁻² step-increased current density in Li|Li_{5.5+3x}Zn_xP_{1-x}O_{4.5-x}Br_{1.5}|Li batteries, where x = (b) 0, (c) 0.02, (d) 0.04, (e) 0.06, (f) 0.08 at 30 °C. (g) Diagram of critical current density (CCD) and electronic conductivity of electrolytes with various ZnO substitutions.

current density (CCD) and electronic conductivity of electrolytes with various ZnO substitutions are shown in Figure 3g. Briefly, electronic conductivity decreases rapidly with increasing ZnO substitution amount. CCD increases rapidly with increasing substitution amount until 4%ZnO and then decreases when additional ZnO substitution proportion. Excessive ZnO introduction results in the impedance increase rapidly, and the ionic conduction is also affected. Decent upper-limit current density corresponds to the improved Li dendrites suppression capability and low overpotential increase in cell cycling. LPSBr_{1.5}-4% ZnO electrolyte owns a more stable dendrite suppression capability, a low electronic conductivity, and a stable interface while contacting with Li metal. ZnO element substitution changes the micro-composition of the interface, therefore, CCD and long-term cycling capability is enhanced.

Air stability is also a vital parameter to assess the practicability of sulfide solid electrolytes (SSEs). The instability of sulfide solid electrolyte stems from the unstable P–S bond, as it can react with moisture and oxygen to produce toxic H₂S gas and lead to the hydrolysis of PS₄³⁻ units and serious

structure decomposition.^[49] The Li_{7-x}PS_{6-x}Cl_x Argyrodite was severely degraded after exposure to moisture for 24 h. Nano crystallites of Li₂CO₃, LiCl, Li₂SO₄, and Li₃PO₄ were formed. Micrometer-size single crystals become polycrystalline, and crystallinity decreases after 1 h of exposure. Poly-crystallization causes an increase in the grain

boundary and a decrease in ionic conductivity.^[50] Indeed, higher humidity is unavoidable in practice. For the sake of verifying the air stability changes in LPSBr_{1.5}-xZnO. The H₂S generation amount is calculated to confirm the structure stability of LPSBr_{1.5}-xZnO. As shown in Figure 4a, the amount of H₂S gas generation is calculated by the following equation:

$$V = \frac{C \times L \times 10^{-6}}{m}$$

where V denotes the total amount of H₂S generation (cm³ g⁻¹) normalized by the weight m of the sulfide electrolyte sample (g), C is the recorded H₂S concentration (ppm), and L is the desiccator volume (cm³).^[49] Although all samples have minor

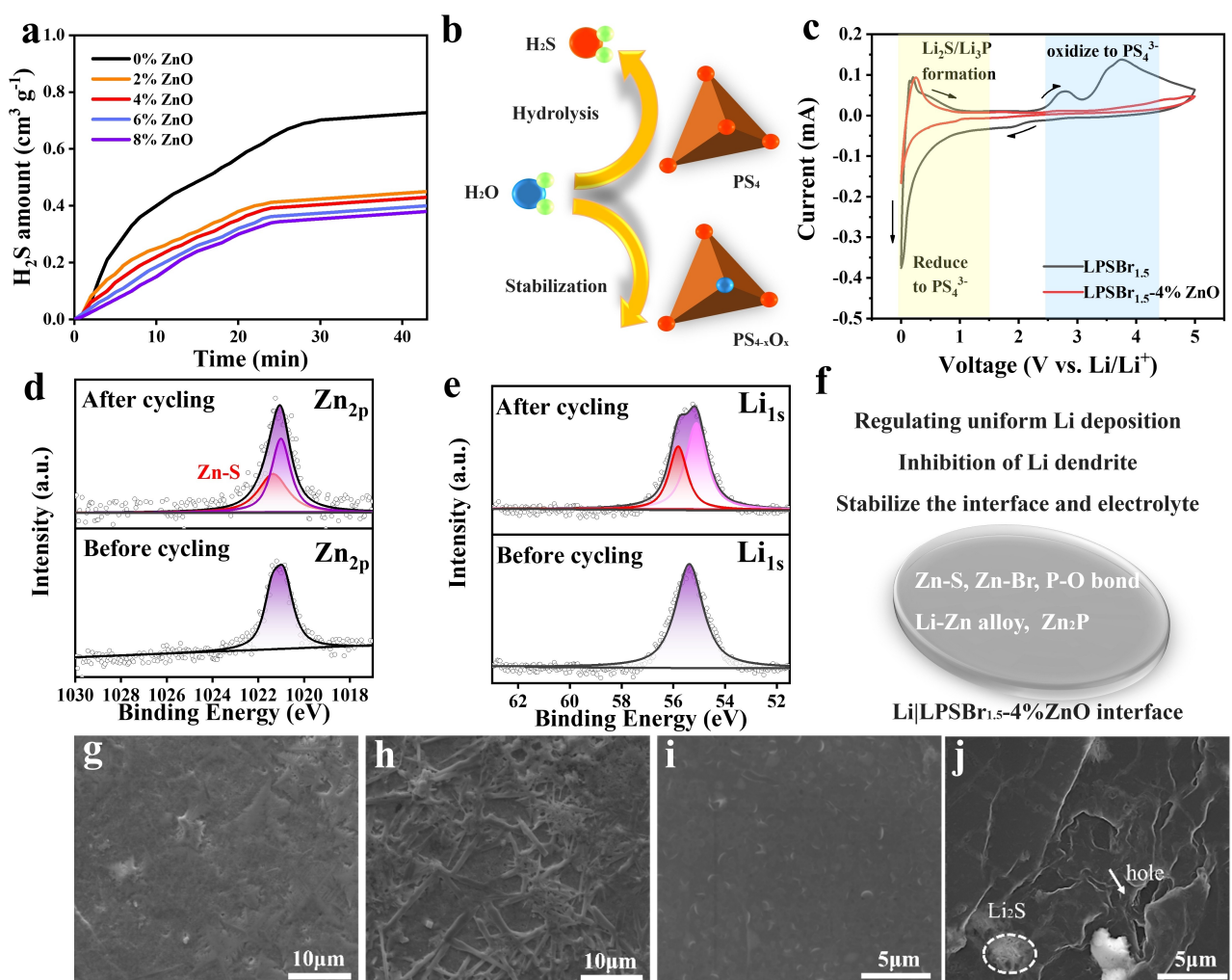


Figure 4. (a) H₂S gas generation performance of pristine and ZnO element substituted SSE at 30% specific humidity air environment. (b) Air stability improvement mechanism schematic. (c) Cyclic voltammetry profile of LPSBr_{1.5}-4%ZnO + VGCF | LPSBr_{1.5}-4%ZnO | Li, LPSBr_{1.5} + VGCF | LPSBr_{1.5} | Li semi-blocking cell with 1 mV S⁻¹. XPS spectra comparison of (d) Li_{1s}, (e) Zn_{2p} before and after Li symmetric cell in LPSBr_{1.5}-4%ZnO electrolyte. SEM image of cycled Li interface in contact with (g) (i) LPSBr_{1.5}-4%ZnO, (h) (j) Li_{5.5}PS_{4.5}Br_{1.5} electrolyte.

vibrations, the whole of $\text{LPSBr}_{1.5}\text{-xZnO}$ electrolytes have shorter rapid H_2S gas generation time, smaller H_2S gas generation amount, and more stable structure by comparison. Therefore, all the $\text{LPSBr}_{1.5}\text{-xZnO}$ ($x > 0$) have a more stable structure and better air stability than the $\text{LPSBr}_{1.5}$. The H_2S gas generation amount increases rapidly in the first several minutes and then reaches the maximum value, in brief, $\text{LPSBr}_{1.5}$ is about 30 min, and $\text{LPSBr}_{1.5}\text{-xZnO}$ ($x > 0$) is only around 25 min. Furthermore, the total H_2S gas generation amount of $\text{LPSBr}_{1.5}\text{-xZnO}$ ($x > 0$) is about half of $\text{LPSBr}_{1.5}$, the former is about $0.35\text{--}0.4 \text{ cm}^3 \text{ g}^{-1}$, the latter is about $0.76 \text{ cm}^3 \text{ g}^{-1}$. Especially, the air stability of $\text{LPSBr}_{1.5}\text{-xZnO}$ SSEs follows the order of $8\% \text{ ZnO} > 6\% \text{ ZnO} > 4\% \text{ ZnO} > 2\% \text{ ZnO}$ (an opposite tendency relationship with H_2S gas generation amount). Respectively, the variance is pretty limited in $\text{LPSBr}_{1.5}\text{-xZnO}$ ($x > 0$) electrolyte, it can be regarded that these electrolytes have the familiar stability at a specific ZnO substitution range. This is consistent with the stability correlation to oxygen amount in electrolyte, oxygen introduction can improve stability.^[51] though the $\text{LPSBr}_{1.5}\text{-8\%ZnO}$ has the best-improved air stability, its low ionic conductivity (1.54 mS cm^{-1}) becomes a restriction for application in ASSBs. As shown in Figure 4b, the air stability improvement mechanism schematic shows that the $\text{PS}_{4-x}\text{O}_x^{3-}$ group can be stable with H_2O , which benefits from the introduction of oxygen. $\text{PS}_{4-x}\text{O}_x^{3-}$ group keeps electrolytes more stable and hardly hydrolyze, and different oxygen amounts have varying stability improvements. Figure S6 shows the $\text{LPSBr}_{1.5}\text{-4\%ZnO}$ XRD patterns before and after 2 h exposure to a humid air environment. All main diffraction peaks keep well, demonstrating the high air stability of $\text{LPSBr}_{1.5}\text{-4\%ZnO}$. Figure S7 shows the H_2S gas detection set. Respectively, the weak P–S bond still exists in the structure of the electrolyte. Therefore, it may not lead to complete moisture stability, oxygen introduction in site-disordered $\text{LPSBr}_{1.5}$ can mitigate the serious moisture stability by several results, which is also good news.

Besides, property-detrimental decomposition forms in interfacial oxidation and reduction during cell cycling, which may increase interface/battery resistance for its ionic insulator nature.^[52] $\text{Li}_6\text{PS}_5\text{Cl}$ is oxidized above $\sim 2.5 \text{ V}$ (vs. Li/Li^+) to form LiCl and Li_2PS_4 , which decompose into P_2S_x ($x \geq 5$) and S_0 upon further oxidation during electrochemical de-lithiation.^[22,52] Interface reaction also occurs during electrochemical lithiation.^[53] As shown in Figure 4c, cyclic voltammogram (CV) measurements are performed on cells to characterize the stability of electrolytes or electrodes by different peak positions and strengths. To detect the interfacial features of $\text{LPSBr}_{1.5}\text{-4\%ZnO}$, Li metal and vapor-grown carbon fiber (VGCF) are used to characterize the stability of electrolytes. VGCF + SSE | SSE | Li cells assembled with $\text{LPSBr}_{1.5}$ and $\text{LPSBr}_{1.5}\text{-4\%ZnO}$ are tested at $0\text{--}5 \text{ V}$ voltage range, with 1 mV s^{-1} . In the curve of $\text{LPSBr}_{1.5} + \text{VGCF} | \text{LPSBr}_{1.5} | \text{Li}$ cell, the high voltage peaks (2.4 V) correspond to the oxidation peak, and low voltage peaks (0.8 V) correspond to the reduction of solid electrolytes respectively. Specifically, the light blue area corresponds to the oxidation of PS_4^{3-} , the light yellow area corresponds to the reduction to PS_4^{3-} and $\text{Li}_2\text{S}/\text{Li}_3\text{P}$ formation, the side-reaction part lower than 0.5 V (vs. Li/Li^+) indicates the interphase generation, including Li_3P , Li_2S , and LiCl .^[54] The curve

of $\text{LPSBr}_{1.5}\text{-4\%ZnO} + \text{VGCF} | \text{LPSBr}_{1.5}\text{-4\%ZnO} | \text{Li}$ cell shows a smaller reduction current at 0.8 V , smaller oxidization current at 2.4 V , and smaller side-reduction current less than 0.5 V , smaller current means more stable structure. It is well demonstrated that $\text{LPSBr}_{1.5}\text{-4\%ZnO}$ is stable towards Li metal and enables the suppression of the interface reactions.

Irreversible solid electrolyte decomposition always occurs in cycling cells, which deteriorates the cell capacity and stability of interphase seriously. To obtain in-depth insight and composition change on the battery interphase layer, X-ray photoelectron spectroscopy (XPS) is applied to characterize the Li interface before and after cycling. XPS spectra comparison of (d) Zn_{2p} , (e) Li_{1s} before and after Li symmetric cell in $\text{LPSBr}_{1.5}\text{-4\%ZnO}$ electrolyte are shown in Figure 4d and Figure 4e. $\text{Li} | \text{LPSBr}_{1.5}\text{-4\%ZnO}$ interface shows single Zn (1021.0 eV) peak before cycling and a new Zn-S (1021.8 eV) peak forms after cycling. Besides, Zn-O (1022.1 eV) has disappeared while electrolyte synthesizing, and never forms again afterwards, which also demonstrates the O substitution to S successfully. The peak at 55.5 eV before cycling is ascribed to Li element. A new peak appears at 56.1 eV in the cycled $\text{Li} | \text{LPSBr}_{1.5}\text{-4\%ZnO}$ interface, which represents the Li–Zn alloy. Zn-S (1021.8 eV) bond and Li-metal alloy peak (56.1 eV) are detected in XPS spectra, which demonstrates the formation of stable interphase.

As shown in Figure 4g–j, SEM images of cycled Li interface with (g) (i) $\text{LPSBr}_{1.5}\text{-4\%ZnO}$ and (h) (j) $\text{Li}_{5.5}\text{PS}_{4.5}\text{Br}_{1.5}$ electrolyte after cell operation. As illustrated in Figure 4g, tiny dendrites can be found in SEM images at the Li surface in contact with $\text{LPSBr}_{1.5}\text{-4\%ZnO}$. In contrast. In Figure 4h, serious dendrites ($15 \mu\text{m}$) form at the Li surface in contact with the $\text{LPSBr}_{1.5}$ electrolyte. Dendrite growth is caused by uneven Li deposition, it can be found that Zn ions alter lithium deposition behavior in interphase, which forms tiny lithium plating sites and promotes uniform lithium deposition. Numerous tiny dendrites are deposited simultaneously, it can be regarded as uniform deposition on the lithium anode approximately. As illustrated in Figure 4i, the $\text{Li} | \text{LPSBr}_{1.5}\text{-4\%ZnO}$ interface exhibits an even interface uniform Li deposition and numerous Li tiny crystals. Moreover, as shown in Figure 4j. Serious side-reaction, side-product, and holes occur in the operated $\text{Li} | \text{LPSBr}_{1.5}$ interface, The light-colored area (white dotted circle) is side-product Li_2S concentration, in addition to several large holes (white arrow point) and electrolyte degradation products in cycled Li surface. In Figure S8, the side-reaction product Li_2S phase can be found in the mapping of (S8a) S, Li_2S is wide-dispersed in cycled $\text{Li} | \text{LPSBr}_{1.5}$ interface, higher content of Li_2S at the interface impedes ionic conductivity and increases the interfacial impedance. As shown in Figure S8b, the mapping image of P indicates the position of stable SSE, due to the basic group of PS_4^{3-} units in electrolytes. It can be demonstrated that a stable solid-electrolyte interphase (SEI) has formed in $\text{Li} | \text{LPSBr}_{1.5}\text{-4\%ZnO}$ interphase, which is proposed to prevent continuous interfacial reaction among electrolyte and Li. In a word, The $\text{LPSBr}_{1.5}\text{-4\%ZnO}$ electrolyte can participate in the formation of a stable interfacial phase, which inhibits interface side reactions and excessive dendrite growth. The surface of the original lithium is flat and smooth with a few machining marks. As

shown in Figure 4f, the interface stability improvement diagram concludes the mechanism, the new formation of Li–Zn, Zn₂P, Zn–Br, Zn–S, P–O alloy or bond is composed of a stable interphase, which is ion-conducted and electro-insulated. The interphase regulates uniform Li deposition, inhibiting Li dendrite, and stabilizing the interface and electrolyte.

Due to the combination with commercial high-voltage metal oxide cathode, all-solid-state battery (ASSB) impedance increase, and capacity fade are induced by partial solid electrolyte decomposition, in addition to the formed interphase around electrode and electrolyte.^[53] To further investigate the underlying mechanism for high charge/discharge capacity, evaluate the electrochemical performance of LPSBr_{1.5} and LPSBr_{1.5}-4%ZnO, and whether ZnO substitution can alleviate the SSE partial decomposition. ASSBs are constructed in a Li–In alloy anode and LiCoO₂ (LCO) cathode mold battery assembly with LPSBr_{1.5} and LPSBr_{1.5}-4%ZnO electrolyte. Figure 5a shows the schematic diagram of ASSB, which is composed of a composite cathode, electrolyte layer, Li–In anode, and two

current collectors (stainless steel pellets). Figure 5b–c shows the charge and discharge curves at varying cycles of LCO|SSE|In-Li. Figure 5b shows ASSB assembly LPSBr_{1.5} with a serious capacity loss at each cycle, which means the obvious interfacial reaction. Contrarily, Figure 5c shows ASSB assembly LPSBr_{1.5}-4%ZnO electrolyte with decent overlapping curves for each cycle, indicating a promising capacity retention in ASSB. In addition, ASSB with LPSBr_{1.5}-4%ZnO possesses a much larger initial charge/discharge capacity (168 mAh g⁻¹/137.8 mAh g⁻¹), and a larger 82.8% initial coulombic efficiency (CE). ASSB with LPSBr_{1.5} electrolyte shows the charge/discharge capacity (164 mAh g⁻¹/133 mAh g⁻¹) and an 81.3% initial coulombic efficiency. Decent performance is due to the appearance of stable Zn–S bond and P–O bond in electrolyte and interface. New bonds improve the electrolyte stability, interface stability and battery performance. As depicted in Figure 5g, LCO|LPSBr_{1.5}|In-Li can only work 10 cycles stably and suffer a serious capacity drop afterward at a voltage range of 2.7–4.3 V (vs. Li/Li⁺). Particularly, discharge capacity shows 133 mAh g⁻¹ for the first cycle, 117.7 mAh g⁻¹

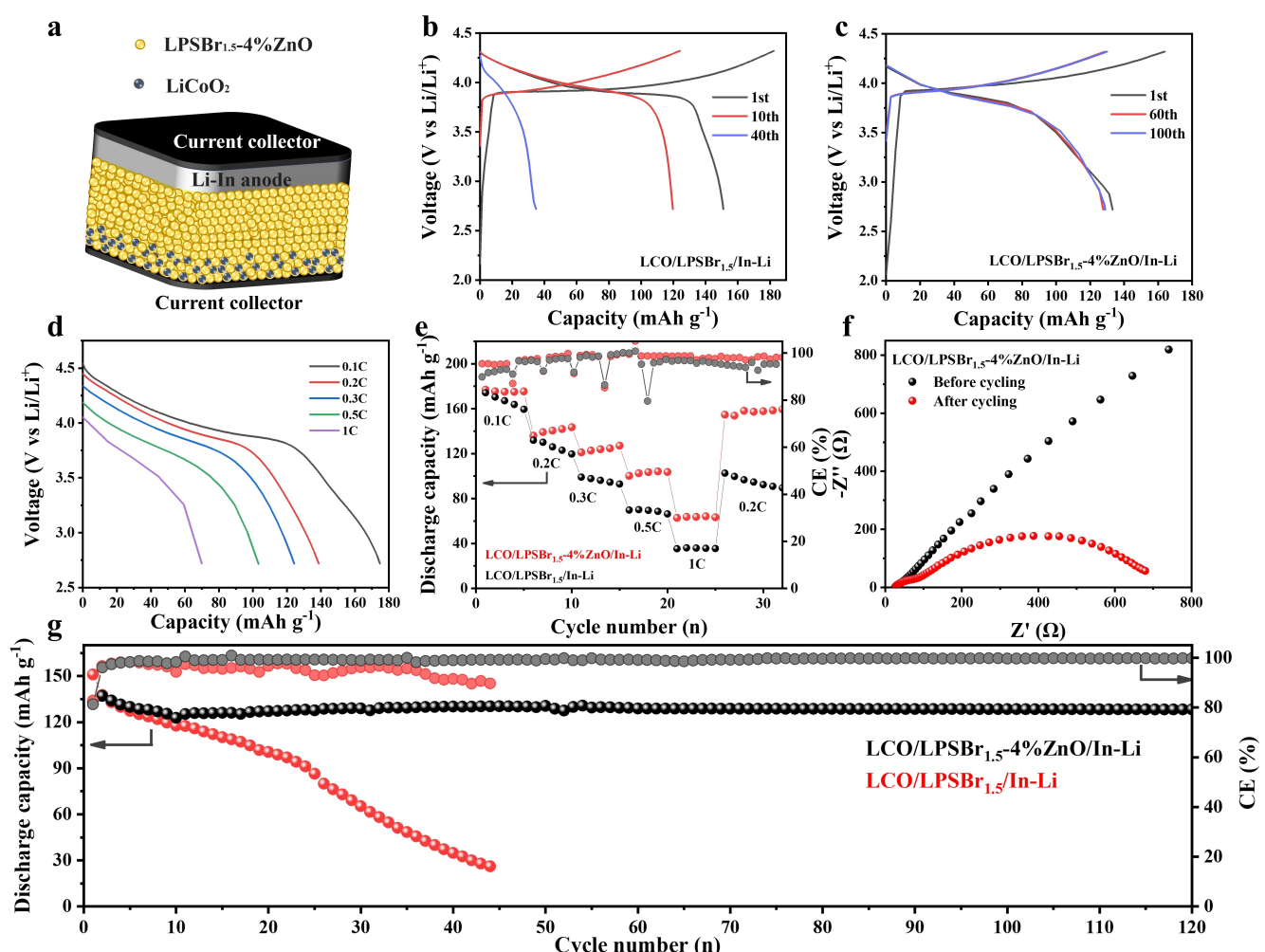


Figure 5. Electrochemical performance of All-Solid-State Battery LCO|SSE|In Li with LPSBr_{1.5} and LPSBr_{1.5}-4%ZnO electrolyte at 60 °C charge and discharge curves at varying cycles (a) Schematic diagram of ASSB with LPSBr_{1.5}-4%ZnO. Charge-discharge profiles comparison of ASSB with (b) LPSBr_{1.5} and (c) LPSBr_{1.5}-4%ZnO electrolyte, at 2.7 V to 4.3 V (vs. Li/Li⁺). (d) Charge-discharge profiles of LPSBr_{1.5}-4%ZnO electrolyte at 2.7–4.6 V (vs. Li/Li⁺) at 0.1 C. (e) the rate capability retention properties in rate cycles for LPSBr_{1.5} and LPSBr_{1.5}-4%ZnO electrolyte at 2.7–4.6 V (vs. Li/Li⁺) at 0.1 C. (f) Nyquist data plots of before and after cycling LCO|LPSBr_{1.5}-4%ZnO|In-Li ASSB. (g) Capacity retention and coulombic efficiency change of ASSB with LPSBr_{1.5} and LPSBr_{1.5}-4%ZnO electrolyte, voltage ranges from 2.7 V to 4.3 V (vs. Li/Li⁺) at 0.1 C.

after 10 cycles, 100.6 mAh g⁻¹ after 20 cycles, 65.3 mAh g⁻¹ after 30 cycles, and only 34.9 mAh g⁻¹ capacity retainment after 40 cycles. Contrarily, LCO|LPSBr_{1.5}-4%ZnO|In-Li has a decent capacity retainment property for more than 120 cycles, and the specific capacity is stabilized at 130 mAh g⁻¹ at 0.1 mA cm⁻² at the same voltage range. The capacity retention rate has reached 93%. As shown in Figure 5f and Figure S9, both initial ASSB with LPSBr_{1.5} and LPSBr_{1.5}-4%ZnO shows about 70 Ω. After cycling, ASSB with LPSBr_{1.5} increases to 10000 Ω and ASSB with LPSBr_{1.5}-4%ZnO shows 700 Ω, suggesting that and Zn—S, P—O, Zn—Br new bonds have formed in electrolyte, new bonds and alloy improve the structure stability, inhibit the electrolyte decomposition and the impedance increase in cell cycling effectively.

Moreover, the inhibition decomposition effect of ZnO also be confirmed by battery performance at a higher voltage range (2.7–4.6 V vs. Li/Li⁺). Rate capability is a crucial indicator to assess capacity recovery capability. The rate capability of ASSB with LPSBr_{1.5} and LPSBr_{1.5}-4%ZnO is characterized by increasing the current density from 0.1 C (0.125 mA cm⁻²), 0.2 C, 0.3 C, 0.5 C, 1 C, then return to 0.2 C, for 5 cycles at every current density. Figure 5d shows the discharge profile of LPSBr_{1.5}-4%ZnO electrolyte at varying current densities. Figure S10 shows the first-cycle charge and discharge curve of the rate test. LCO|LPSBr_{1.5}|In-Li shows about 12% irreversible capacity from the electrolyte partial decomposition. In contrast, LCO|LPSBr_{1.5}-4%ZnO|In-Li shows about 7% irreversible capacity of total charge capacity at 2.7–4.6 V (vs. Li/Li⁺). ASSBs with LPSBr_{1.5}-4%ZnO only have a slight capacity loss compared to the fresh cell, because the partial electrolyte decomposition product is composed of the solid electrolyte interphase (SEI), SEI can stabilize the interface between electrode and electrolyte. Besides, ZnO can inhibit the LPSBr_{1.5} electrolyte decomposition. Therefore, long-term cycle stability enhancement of electrolytes is improved by ZnO element substitution in ASSB. As shown in Figure 5e, the average discharge capacities of ASSB with LPSBr_{1.5}-4%ZnO exhibits specific capacity of 174.1 mAh g⁻¹, 140.5 mAh g⁻¹, 123.9 mAh g⁻¹, 102.5 mAh g⁻¹, 63.7 mAh g⁻¹ at 0.1 C, 0.2 C, 0.3 C, 0.5 C, 1 C, and 154.7 mAh g⁻¹ at 0.2 C, exhibiting a decent rate capability and capacity recoverability. ASSB with LPSBr_{1.5} exhibits specific capacity of 167.1 mAh g⁻¹, 126 mAh g⁻¹, 96 mAh g⁻¹, 69 mAh g⁻¹, 36 mAh g⁻¹, at 0.1 C, 0.2 C, 0.3 C, 0.5 C, 1 C, and 99 mAh g⁻¹ at 0.2 C. Capacity decay occurs seriously in ASSB due to interface side-reaction. This further proves that ZnO element substitution enables decent rate capability and capacity reversibility capability. ZnO can improve the electrolyte structure stability, crystal parameter, interface stability, and stability to high voltage. There is no other side effect on Li_{5.5}PS_{4.5}Br_{1.5} electrolyte or battery performance. SEM images for composite cathode with corresponding EDS mappings of P, S, Co, and O were exhibited in Figure S11.

The electrochemical decomposition and interfacial reactions begin when the electrolyte is subjected to potential over itself electrochemical stability window,^[22] and decomposition stems from limited stability with high voltage cathodes, such as NCM811, and LiCoO₂ (LCO). Therefore, ASSB is assembled with LPSBr_{1.5} and LPSBr_{1.5}-4%ZnO electrolytes with LCO and NCM811

cathode, to detect reduction/oxidation behavior variation. Figure S12 shows first-cycle cyclic voltammogram profiles of LPSBr_{1.5} and LPSBr_{1.5}-4%ZnO with the (S12a) LCO cathode, and Figure S12b presents CV curves of LPSBr_{1.5} and LPSBr_{1.5}-4%ZnO with the NCM811 cathode. Both of the above curves indicate that the CV curves of LPSBr_{1.5}-4%ZnO have lower current and current peaks assembled with different cathodes, proving that the ZnO-substituted electrolyte has a more stable structure and less interfacial side-products.

Conclusions

In this work, a series of Li_{5.5+3x}Zn_xP_{1-x}O_xS_{4.5-x}Br_{1.5} sulfide electrolytes have been achieved through the ball milling-sintering-milling method, which still keeps the original crystal structure and superior ionic conductivity. At the same time, electrochemical stability and chemical stability are enhanced by ZnO element substitution. Li_{5.62}Zn_{0.04}P_{0.96}O_{0.04}S_{4.46}Br_{1.5} (LPSBr_{1.5}-4%ZnO) exhibits the most promising performance among all substitution amounts. The ionic conductivity is found to be 2.25 mS cm⁻¹ at room temperature, as well as 1.17×10⁻⁸ S cm⁻¹ electronic conductivity, Li symmetric cell with LPSBr_{1.5}-4%ZnO can continue cycling for more than 800 h at 0.1 mA cm⁻². The critical current density reaches 1.4 mA cm⁻² at 30°C, which demonstrates good lithium compatibility, dendrite suppression ability, and an even Li plating/stripping procession. ASSB with LPSBr_{1.5}-4%ZnO enables excellent electrochemical performance, which can cycle with 130 mAh g⁻¹ capacity retainment of more than 120 cycles in LCO|SSE|In-Li cell. Performance enhancement originates from ZnO element substitution. ZnO changes the crystal cell parameter of electrolyte and interface composition, provides a more stable crystal structure and interface, and compresses the dendrite growth. In conclusion, the ZnO element substitution strategy is a promising pathway to improve the electrochemical stability and chemical stability of site-disorder Argyrodite electrolytes.

Experimental Section

The Experimental Section is available in the Supporting information.

Acknowledgements

Financial supports from the National Key R&D Program of China (2022YFB3803505), National Natural Scientific Foundation of China (U21A2080), Shanxi key research and development program (202102060301011), Natural Science Foundation of Beijing Municipality (Z200011) and Fundamental Research Funds for the Central Universities (GJJ2022-03) are gratefully acknowledged.

Conflict of Interests

The authors declare no conflict of interest.

Data Availability Statement

The data that support the findings of this study are available in the supplementary material of this article.

Keywords: All-solid-state battery · Argyrodite electrolyte · element substitution · air stability · interface

- [1] L.-Z. Fan, H. He, C.-W. Nan, *Nat. Rev. Mater.* **2021**, *6*, 1003.
- [2] S. Xia, X. Wu, Z. Zhang, Y. Cui, W. Liu, *Chem* **2019**, *5*, 753.
- [3] X. Fan, C. Wang, *Chem. Soc. Rev.* **2021**, *50*, 10486.
- [4] S. J. Tan, W. P. Wang, Y. F. Tian, S. Xin, Y. G. Guo, *Adv. Funct. Mater.* **2021**, *31*, 2105253.
- [5] L. Li, H. Duan, J. Li, L. Zhang, Y. Deng, G. Chen, *Adv. Energy Mater.* **2021**, *11*, 2003154.
- [6] J. A. Lewis, K. A. Cavallaro, Y. Liu, M. T. McDowell, *Joule* **2022**, *6*, 1418.
- [7] H. Liu, X.-B. Cheng, J.-Q. Huang, H. Yuan, Y. Lu, C. Yan, G.-L. Zhu, R. Xu, C.-Z. Zhao, L.-P. Hou, *ACS Energy Lett.* **2020**, *5*, 833.
- [8] C. Yu, F. Zhao, J. Luo, L. Zhang, X. Sun, *Nano Energy* **2021**, *83*, 105858.
- [9] Q. Zhang, D. Cao, Y. Ma, A. Natan, P. Aurora, H. Zhu, *Adv. Mater.* **2019**, *31*, 1901131.
- [10] N. Kamaya, K. Homma, Y. Yamakawa, M. Hirayama, R. Kanno, M. Yonemura, T. Kamiyama, Y. Kato, S. Hama, K. Kawamoto, *Nat. Mater.* **2011**, *10*, 682.
- [11] Y. Kato, S. Hori, T. Saito, K. Suzuki, M. Hirayama, A. Mitsui, M. Yonemura, H. Iba, R. Kanno, *Nat. Energy* **2016**, *1*, 1.
- [12] Y. Li, S. Song, H. Kim, K. Nomoto, H. Kim, X. Sun, S. Hori, K. Suzuki, N. Matsui, M. Hirayama, *Science* **2023**, *381*, 50.
- [13] A. E. Maughan, Y. Ha, R. T. Pekarek, M. C. Schulze, *Chem. Mater.* **2021**, *33*, 5127.
- [14] C. Yu, S. Ganapathy, E. V. Eck, L. V. Eijck, M. Wagemaker, *J. Mater. Chem. A* **2017**, *5*, 21178.
- [15] C. Yu, Y. Li, M. Willans, Y. Zhao, K. R. Adair, F. Zhao, W. Li, S. Deng, J. Liang, M. N. Banis, *Nano Energy* **2020**, *69*, 104396.
- [16] X. Feng, P.-H. Chien, Y. Wang, S. Patel, P. Wang, H. Liu, M. Immediato-Scuotto, Y.-Y. Hu, *Energy Storage Mater.* **2020**, *30*, 67.
- [17] Y. Liu, H. Peng, H. Su, Y. Zhong, X. Wang, X. Xia, C. Gu, J. Tu, *Adv. Mater.* **2022**, *34*, 2107346.
- [18] A. Gautam, M. Sadowski, M. Ghidu, N. Minafra, A. Senyshyn, K. Albe, W. G. Zeier, *Adv. Energy Mater.* **2021**, *11*, 2003369.
- [19] A. Gautam, M. Ghidu, E. Suard, M. A. Kraft, W. G. Zeier, *ACS Appl. Energ. Mater.* **2021**, *4*, 7309.
- [20] C. Yu, Y. Li, W. Li, K. R. Adair, X. Sun, *Energy Storage Mater.* **2020**, *30*, 328.
- [21] W. Fitzhugh, F. Wu, L. Ye, W. Deng, P. Qi, X. Li, *Adv. Energy Mater.* **2019**, *9*, 1900807.
- [22] D. H. Tan, E. A. Wu, H. Nguyen, Z. Chen, M. A. Marple, J.-M. Doux, X. Wang, H. Yang, A. Banerjee, Y. S. Meng, *ACS Energy Lett.* **2019**, *4*, 2418.
- [23] X. Zhu, L. Cheng, H. Yu, F. Xu, W. Wei, L.-Z. Fan, *Journal of Materomics* **2022**, *8*, 649.
- [24] Z. Zhang, L. Zhang, X. Yan, H. Wang, Y. Liu, C. Yu, X. Cao, L. van Eijck, B. Wen, *J. Power Sources* **2019**, *410*, 162.
- [25] G. Liu, J. Shi, M. Zhu, W. Weng, L. Shen, J. Yang, X. Yao, *Energy Storage Materials* **2021**, *38*, 249.
- [26] X. Liu, X. Li, H. Li, H. B. Wu, *Chemistry-A European Journal* **2018**, *24*, 18293.
- [27] Y. Zheng, Y. Yao, J. Ou, M. Li, D. Luo, H. Dou, Z. Li, K. Amine, A. Yu, Z. Chen, *Chem. Soc. Rev.* **2020**, *49*, 8790.
- [28] L. Ye, X. Li, *Nature* **2021**, *593*, 218.
- [29] L. Zhou, N. Minafra, W. G. Zeier, L. F. Nazar, *Acc. Chem. Res.* **2021**, *54*, 2717.
- [30] H. Liu, Q. Zhu, Y. Liang, C. Wang, D. Li, X. Zhao, L. Gao, L.-Z. Fan, *Chem. Eng. J.* **2023**, *462*, 142183.
- [31] H. Liu, Q. Zhu, C. Wang, G. Wang, Y. Liang, D. Li, L. Gao, L. Z. Fan, *Adv. Funct. Mater.* **2022**, *32*, 2203858.
- [32] Y. Ni, C. Huang, H. Liu, Y. Liang, L. Z. Fan, *Adv. Funct. Mater.* **2022**, *32*, 2205998.
- [33] T. Chen, D. Zeng, L. Zhang, M. Yang, C. Yu, *J. Energy Chem.* **2020**, *59*, 530.
- [34] Y. Li, J. Li, J. Cheng, X. Xu, L. Chen, L. Ci, *Adv. Mater. Interfaces* **2021**, *8*, 2100368.
- [35] N. Ahmad, L. Zhou, M. Faheem, M. K. Tufail, W. Yang, *ACS Appl. Mater. Interfaces* **2020**, *12*, 21548.
- [36] X. Zhu, H. Yu, L. Cheng, F. Xu, Z. Wang, L.-Z. Fan, *Journal of Materomics* **2023**, *9*, 82.
- [37] A. Hayashi, H. Muramatsu, T. Ohtomo, S. Hama, M. Tatsumisago, *J. Mater. Chem. A* **2013**, *1*, 6320.
- [38] G. Liu, D. Xie, X. Wang, X. Yao, S. Chen, R. Xiao, H. Li, X. Xu, *Energy Storage Materials* **2019**, *17*, 266.
- [39] A. Hayashi, H. Muramatsu, T. Ohtomo, S. Hama, M. Tatsumisago, *Journal of Alloys and Compounds* **2014**, *591*, 247.
- [40] Z. Sun, Y. Lai, N. Lv, Y. Hu, B. Li, L. Jiang, J. Wang, S. Yin, K. Li, F. Liu, *ACS Appl. Mater. Interfaces* **2021**, *13*, 54924.
- [41] B. W. Taklu, W. N. Su, Y. Nikodimos, K. Lakshmanan, N. T. Temesgen, P. X. Lin, S. K. Jiang, C. J. Huang, D. Y. Wang, H. Sheu, *Nano Energy* **2021**, *90*, 106542.
- [42] T. Chen, L. Zhang, Z. Zhang, P. Li, B. Xu, *ACS Appl. Mater. Interfaces* **2019**, *2019* (*11*), 40808.
- [43] Z. Jiang, Y. Liu, H. Peng, J. Li, X. Xu, H. Su, Y. Zhong, X. Wang, C. Gu, J. Tu, *Energy Storage Mater.* **2023**, *56*, 300.
- [44] L. Peng, S. Chen, C. Yu, *ACS Appl. Mater. Interfaces* **2022**, *14*, 4179.
- [45] G. Li, S. Wu, H. Zheng, Y. Yang, J. Cai, H. Zhu, X. Huang, H. Liu, H. Duan, *Adv. Funct. Mater.* **2023**, *33*, 2211805.
- [46] R. Song, J. Yao, R. Xu, Z. Li, X. Yan, C. Yu, Z. Huang, L. Zhang, *Adv. Energy Mater.* **2023**, *13*, 2203631.
- [47] F. Han, A. S. Westover, J. Yue, X. Fan, F. Wang, M. Chi, D. N. Leonard, N. J. Dudney, H. Wang, C. Wang, *Nat. Energy* **2019**, *4*, 187.
- [48] P. Lu, Y. Xia, Y. Huang, Z. Li, Y. Wu, X. Wang, G. Sun, S. Shi, Z. Sha, L. Chen, *Adv. Funct. Mater.* **2023**, *33*, 2211211.
- [49] P. Lu, D. Wu, L. Chen, H. Li, F. Wu, *Electrochim. Energy Rev.* **2022**, *5*, 3.
- [50] H. Tsukasaki, H. Sano, K. Igashira, A. Wakui, T. Yaguchi, S. Mori, *J. Power Sources* **2022**, *524*, 231085.
- [51] S. Shim, W. B. Park, J. Han, J. Lee, B. D. Lee, J. W. Lee, J. Y. Seo, S. R. Prabakar, S. C. Han, S. P. Singh, *Adv. Sci.* **2022**, *9*, 2201648.
- [52] T. K. Schwietert, V. A. Arszelewskia, C. Wang, C. Yu, A. Vasileiadis, N. J. de Klerk, J. Hageman, T. Hupfer, I. Kerkamm, Y. Xu, *Nat. Mater.* **2020**, *19*, 428.
- [53] S. Wenzel, S. J. Sedlmaier, C. Dietrich, W. G. Zeier, J. Janek, *Solid State Ionics* **2018**, *318*, 102.
- [54] C. Liu, B. Chen, T. Zhang, J. Zhang, R. Wang, J. Zheng, Q. Mao, X. Liu, *Angew. Chem.* **2023**, *62*, e202302655.
- [55] J. Auvergniot, A. Cassel, J. B. Ledeuil, V. Viallet, R. Dedryvère, *Chem. Mater.* **2017**, *29*, 3883.

Manuscript received: January 24, 2024

Revised manuscript received: March 21, 2024

Accepted manuscript online: March 25, 2024

Version of record online: April 19, 2024